Nonresonant Raman scattering in extremely correlated Fermi liquids

Peizhi Mai and B. Sriram Shastry
Physics Department, University of California, Santa Cruz, California 95064, USA

(Received 24 May 2018; revised manuscript received 1 August 2018; published 4 September 2018)

We present theoretical results for the optical conductivity and the nonresonant Raman susceptibilities for three principal polarization geometries relevant to the square lattice. The susceptibilities are obtained using the recently developed extremely correlated Fermi liquid theory for the two-dimensional t-t'-J model, where t and t' are the nearest- and second-neighbor hopping. Our results sensitively depend on t, t'. By studying this quartet of related dynamical susceptibilities, and their dependence on t, t', doping, and temperature, we provide a useful framework of interpreting and planning future Raman experiments on strongly correlated matter.

DOI: 10.1103/PhysRevB.98.115101

I. INTRODUCTION

Inelastic or Raman scattering of electrons by photons (e-γ) in strongly correlated systems is of considerable current interest. The scattering intensity, given by the Kramers-Heisenberg formula [1], consists of a resonant and a nonresonant piece. The nonresonant piece depends only on the energy transfer. In contrast, the resonant piece also depends on the incident energy, and it is the focus of this work. In typical weakly correlated metals, this contribution is confined to a small energy window of a few meV [2,3]. Raman scattering theory, if based solely on density fluctuations, would give a vanishing contribution as $q \to 0$ due to the conservation law in that limit. The early works of Refs. [2,4] showed that nonparabolic bands lead to the coupling of light to a nonconserved operator (the stress tensor operators discussed below), rather than the density. These operators are exempt from conservation laws that govern the density, and therefore they can lead to nonresonant Raman scattering.

Recent experiments [5–17] in strongly correlated metallic systems such as high-T_c superconductors have added further complexity to challenge to our understanding. It is found that the scattering is q-independent and extends over a much larger energy range O (eV), and it is also observed to have a complex T dependence [5–7,10,14]. To explain these, a systematic reformulation of light scattering in narrowband systems was developed in [18–23]. Shastry and Shraiman (SS) [18,19] developed a theory of Raman scattering in Mott-Hubbard systems using the Hubbard model, where nonparabolicity of bands is built in correctly, so that the conservation law concerns are taken care of. However, the large energy spread of the nonresonant signals remains unaccounted for. It cannot arise from quasiparticles in Fermi liquids, and hence SS argued that a large contribution from the incoherent background of the electron spectral function is required to explain the data (see, e.g., [5,6]). This qualitative argument is not fine enough to explain or predict differences in backgrounds in different geometries. The latter remains an unresolved problem, and it is the focus of the present work.

Progress toward a solution at the microscopic level has been slow since a suitable theory in two dimensions displaying such a phenomenon has been lacking so far. In this work, we apply the recently developed extremely correlated Fermi liquid theory (ECFL) [24,25] to calculate the Raman cross sections using the k-dependent bare vertices of Refs. [18,19]. This theory provides a framework for controlled calculations in the t-J model, a prototypical model for very strong correlations, and a limiting case of the Hubbard model. The theory has been successfully benchmarked against essentially exact results in $d = 0$ [26], $d = 1$ [27], as well as $d = \infty$ [28]. A recent application of the theory to the physically important case of $d = 2$ in Refs. [29,30] gives detailed results for the spectral functions and the resistivity ρ in the t-t'-J model, with nearest- and second-neighboring hopping. The state obtained in ECFL at low hole densities has a very small quasiparticle weight $Z \ll 1$. A significant result is that the temperature dependence of resistivity is nonquadratic already at $T \sim 100$ K for low hole doping.

In this work, we apply the solution found in Refs. [29,30] to compute the Raman scattering, in three standard polarization configuration channels A_{1g}, B_{1g}, B_{2g} defined below [31]. The results are applicable to either electron doping or hole-doped cuprates by choosing the sign of t', and they may apply to other strongly correlated systems as well. Following SS, we also compare the Raman conductivities with the optical conductivity, and we shall focus on the quartet of these results on various values of material parameters.

The utility of comparing the optical conductivity with the Raman response requires a comment. SS [18,19] suggested that this comparison is useful, since these are exactly related in a limiting situation of $d = \infty$. Further, in $d = 2, 3, \ldots$ one often calculates the response within the bubble diagrams, where again these are related. In the bubble approximation, also used in the present work, one evaluates the current-current and related correlation functions by retaining only the lowest-order $\chi_{\rm JJ} \sim \sum_k (\gamma_k)^2 G(k) G(k)$ (i.e., bubble) terms with dressed Green's functions and suitable bare vertices γ. While this calculation misses a contribution due to the renormalization of one of the bare vertices $\gamma \to \Gamma$, it is hard to improve on

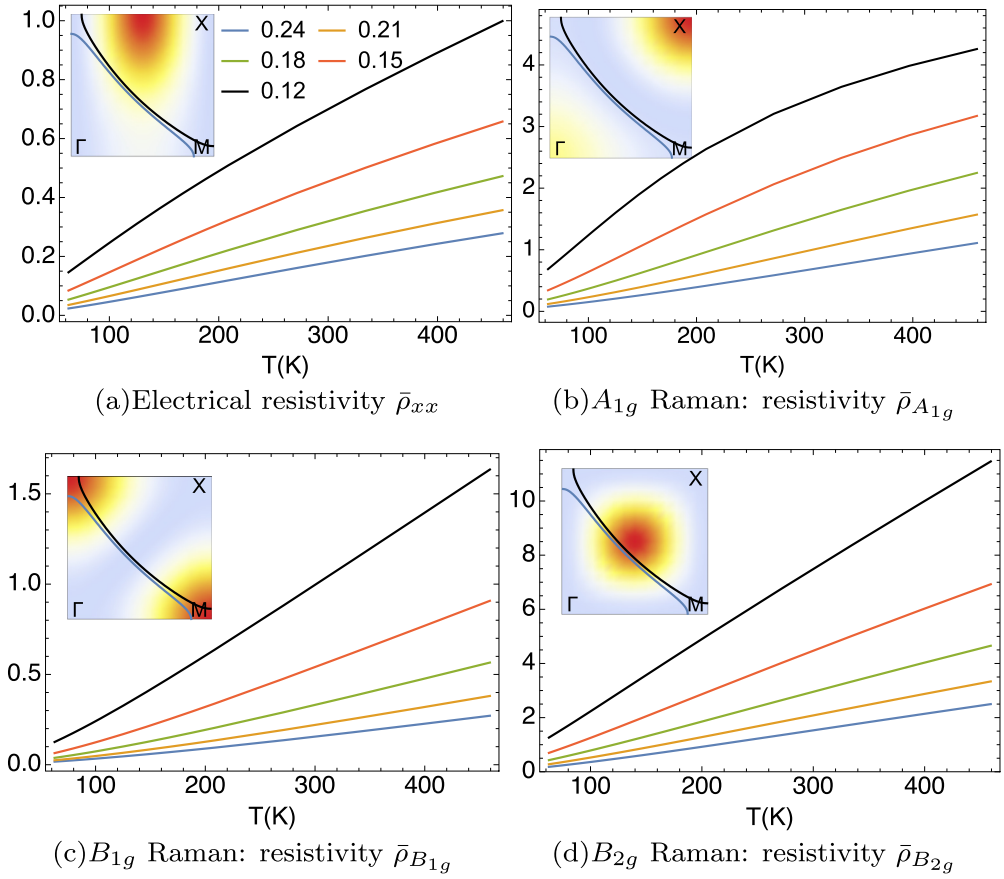

FIG. 1. Electrical and Raman resistivities from Eq. (5) at $t' = -0.2$ with varying hole doping δ, as marked. The T dependence of electrical resistivity and the A_{1g} resistivity are concave-down at small δ, while the B_{1g} and B_{2g} resistivity are flat or concave-up. Inset: The displayed Fermi surfaces at $\delta = 0.12, 0.24$ locate the maxima of $\Upsilon(k, \omega)$. The relevant squared vertices from Eq. (2) are shown as a heat map. The hot spots are movable by varying t' and t.

this already difficult calculation for strong correlations, since G is highly nontrivial. An exception is the special case of $d \to \infty$, where the vertex corrections vanish. Within the bubble scheme, the bare Raman and current vertices are different while everything else is the same. Therefore, one should be able to relate the two experimental results and explore the differences arising from the bare vertices. The "pseudo-identity" of the transport and Raman resistivities has been explored experimentally in Ref. [8] and finds some support. In this work, we use the correct bare vertices in the different geometries to explore the various Raman resistivities to refine the theory. These different bare vertices have a different dependence on the hopping parameters t, t', and the calculations reflect these in specific and experimentally testable ways.

The neglect of vertex corrections also leads to a relationship between various Raman susceptibilities at finite ω. In the experiments of Ref. [6], the same quartet of susceptibilities has been studied and found to have a roughly similar scale for their ω dependence, although the curve shapes are distinct. On the theoretical side, one interesting aspect of the results of Refs. [29,30] is that the Fermi surface *shape* remains very close to that of the noninteracting tight-binding model, while of course conserving the area. Thus the Dyson self-energy is a weak function of $\vec{k}$, unlike the strong dependence in one dimension [27]. This fact implies that the vertex corrections, while nonzero, are modest.

II. THE RAMAN AND CURRENT VERTICES

We use the t-t'-J model with a tight-binding dispersion [29] on the square lattice $\varepsilon(k) = -2t[\cos(k_x) + \cos(k_y)] - 4t' \cos(k_x)\cos(k_y)$, and we set the lattice constant $a_0 \to 1$. The photons modulate the Peierls hopping factors as $t_{ij} \to t_{ij} \exp\{ie/\hbar \int_i^j d\vec{r}.\vec{A}\}$, and the second-order expansion coefficients define the scattering operators. In this case, they are

$$\widehat{\mathcal{J}}_{\alpha,q} = \sum_{k\sigma} \mathcal{J}_\alpha(k) C^\dagger_{k+\frac{1}{2}q,\sigma} C_{k-\frac{1}{2}q,\sigma}, \tag{1}$$

where α is a composite index determined by the in-out polarizations of the photon. With that the vertices $\mathcal{J}_\alpha$ for the three main Raman channels are

$$\begin{aligned} A_{1g}&: \ \mathcal{J}_{A_{1g}}(k) = 2t(\cos k_x + \cos k_y) + 4t' \cos k_x \cos k_y, \\ B_{1g}&: \ \mathcal{J}_{B_{1g}}(k) = 2t(\cos k_x - \cos k_y), \\ B_{2g}&: \ \mathcal{J}_{B_{2g}}(k) = -4t' \sin k_x \sin k_y, \\ xx&: \ \mathcal{J}_{xx}(k) = 2 \sin k_x (t + 2t' \cos k_y). \end{aligned} \tag{2}$$

The definition of $\alpha = xx$ corresponds to the particle current along x. It integrates the charge current into the same scheme

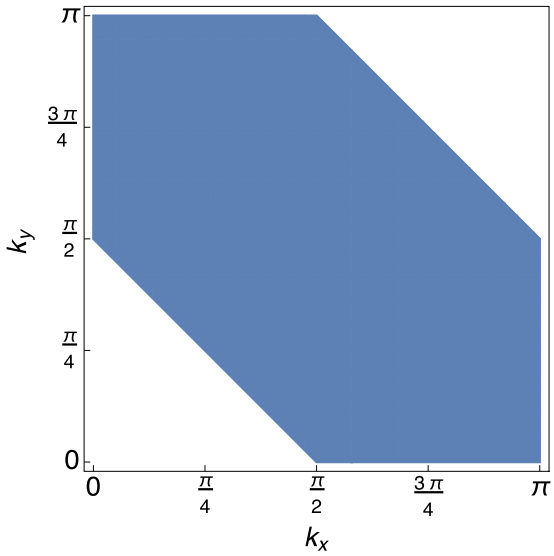

FIG. 2. Shaded region for estimating the average scale of the vertices.

as the Raman scattering. It is interesting that the B_{2g} vertex is independent of t, and is solely governed by t'. The vertex B_{1g} is complementary given its independence of t'. These geometries sample different parts of k space in interesting ways due to their different $\vec{k}$ dependences.

We next define the calculated variables, and we display the results for them from computations based on the spectral functions found in Refs. [29,30]. Results in the $\omega = 0$ dc limit and also at finite ω are shown. Finally, we discuss the results and their significance.

III. RAMAN AND CHARGE SUSCEPTIBILITIES

We summarize the formulas for the (nonresonant) Raman susceptibility, and in the spirit of Refs. [18,19] we also define a *Raman conductivity and resistivity* in analogy as follows:

$$\chi_\alpha(q,z) = \sum_{nm} \frac{p_n - p_m}{\epsilon_m - \epsilon_n - z} |(\widehat{\mathcal{J}}_{\alpha,q})_{n,m}|^2, \tag{3}$$

where p_n is the probability of the state n. For visible light, $qa_0 \ll 1$ and therefore we set $q \to 0$. The (nonresonant) Raman intensity $\mathcal{I}_\alpha$ [1–3,18,19] and the Raman conductivities [18,19] are given by

$$\mathcal{I}_\alpha(0,\omega) = \frac{\chi''_\alpha(0,\omega)}{(1-e^{-\beta\omega})}, \quad \sigma_\alpha(\omega) = \zeta_\alpha \frac{\chi''_\alpha(0,\omega)}{N_s\omega}, \tag{4}$$

with N_s the number of sites, and $\zeta_{xx} = e^2$ accounting for the electric charge in the conductivity with all other $\zeta_\alpha = 1$. In the

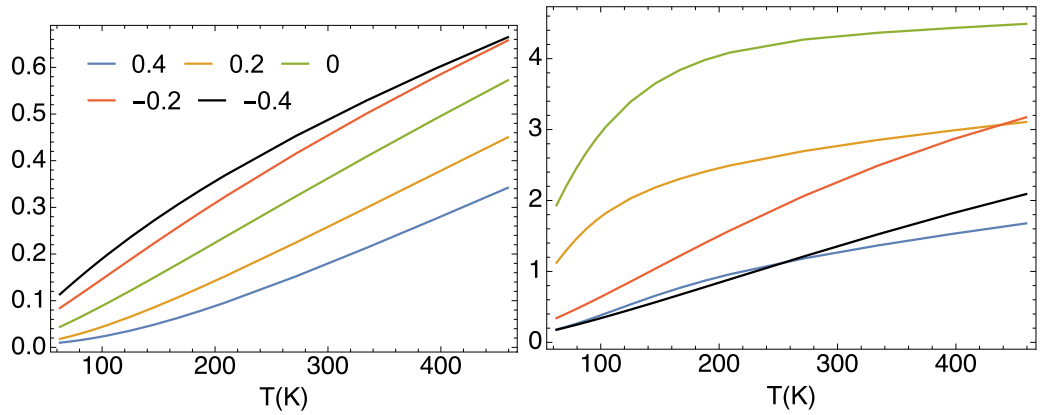

(a)Electrical resistivity $\bar{\rho}_{xx}$ (b)A_{1g} Raman: resistivity $\bar{\rho}_{A_{1g}}$

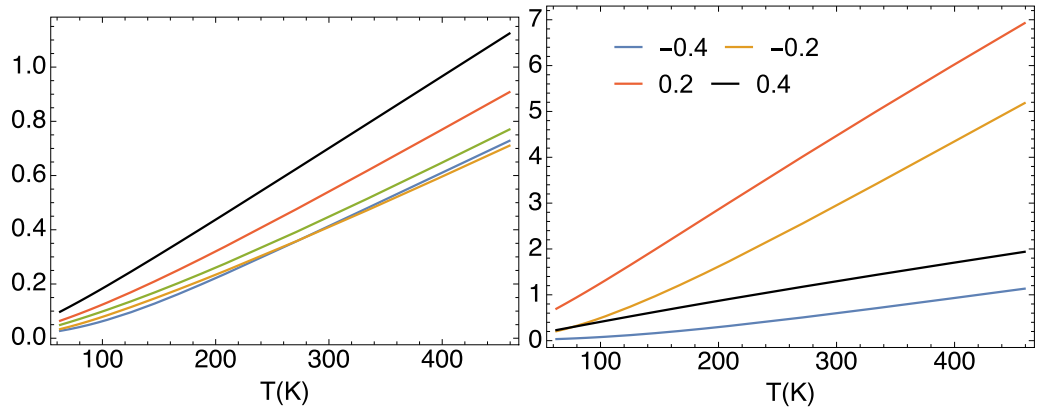

(c)B_{1g} Raman: resistivity $\bar{\rho}_{B_{1g}}$ (d)B_{2g} Raman: resistivity $\bar{\rho}_{B_{2g}}$

FIG. 3. Dimensionless $\bar{\rho}_{xx}$ (taken from Ref. [29]), $\bar{\rho}_{A_{1g}}$, $\bar{\rho}_{B_{1g}}$, and $\bar{\rho}_{B_{2g}}$ at $\delta = 0.15$ with varying second-neighbor hopping t', as marked (same legend for all subfigures). Reference [8] displays data corresponding to the B_{1g} geometry.

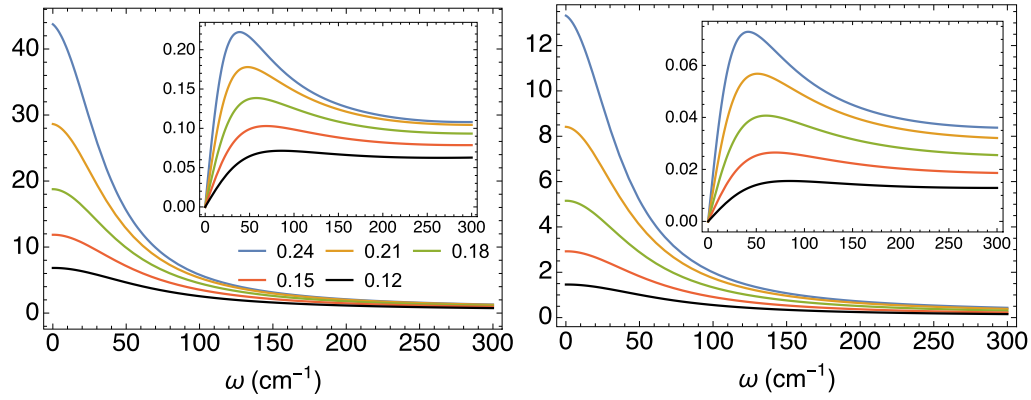

(a)Optical conductivity $\bar{\sigma}_{xx}$ and susceptibility $\bar{\chi}''_{xx}$ (inset) (b)A_{1g} Raman: $\bar{\sigma}_{A_{1g}}$ and $\bar{\chi}''_{A_{1g}}$ (inset)

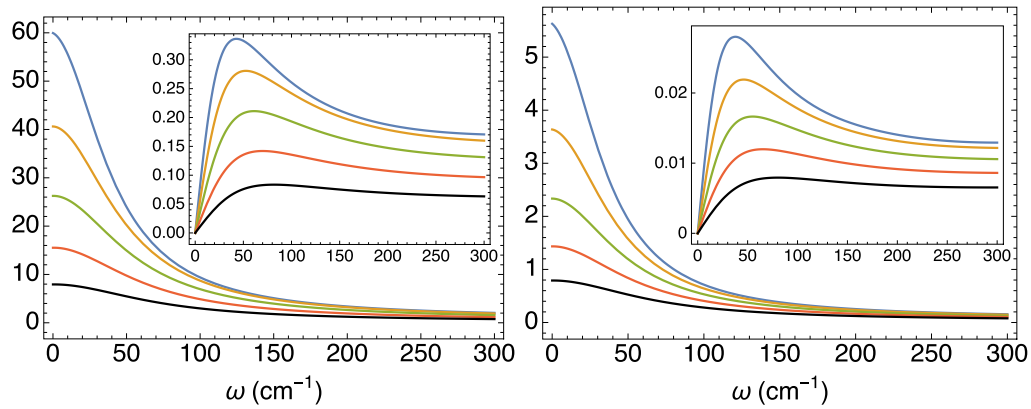

(c)B_{1g} Raman: $\bar{\sigma}_{B_{1g}}$ and $\bar{\chi}''_{B_{1g}}$ (inset) (d)B_{2g} Raman: $\bar{\sigma}_{B_{2g}}$ and $\bar{\chi}''_{B_{2g}}$ (inset)

FIG. 4. Dynamical conductivities $\bar{\sigma}_\alpha$ and susceptibilities $\bar{\chi}''_\alpha$ (inset) for the hole-doped case $t' = -0.2$, $T = 63$ K at different δ, as marked. In the experiments in Ref. [6] (Fig. 1), the same quartet of results is shown for LSCO. At the highest energy of over 1000 K, as in the data, the susceptibility shows no sign of dropping off.

dc limit we define the Raman resistivities

$$\rho_\alpha(0) = \frac{N_s}{\zeta_\alpha}\frac{k_B T}{\mathcal{I}_\alpha(0,0)}, \tag{5}$$

where for $\alpha = xx$, ρ_α is the usual resistivity.

The "pseudo-identity," a statement of universality relating electrical transport and the dc limit of Raman intensities noted by SS in Refs. [18,19], is arrived at if we assume that ρ_α has a similar T dependence for all α: $\mathcal{I}_\alpha(0,0) \sim C_\alpha \frac{T}{\rho_{xx}(T)}$, where C_α is an α-dependent constant. Thus $\rho \sim T^\sigma$ behavior would give rise to $T^{1-\sigma}$ behavior for the Raman intensity in all channels. We see in Fig. 1 that this suggestion is true for the A_{1g} resistivity at hole dopings, but it needs to be adjusted to the different k-dependent filters that make the B_{1g} and B_{2g} channels different from the others. Thus we limit the universality of the pseudo-identity in this work, and we quantify the effects of the bare vertices in the relationship between the members of the quartet of susceptibilities.

Proceeding further using the bubble scheme we get the imaginary part of the dimensionless susceptibility $\bar{\chi}''_\alpha(0,\omega) \equiv \frac{c_0 h}{N_s}\chi''_\alpha(0,\omega)$ as

$$\bar{\chi}''_\alpha(0,\omega) = \omega\left\langle \Upsilon(k,\omega)\mathcal{J}^2_\alpha(k)\right\rangle_k, \tag{6}$$

where $c_0 \sim 6.64$ Å is a typical interlayer separation [29]. The angular average is $\langle A\rangle_k \equiv \frac{1}{N_s}\sum_k A(k)$ and the momentum resolved relaxation scale is

$$\Upsilon(k,\omega) = \frac{4\pi^2}{\omega}\int_{-\infty}^{\infty} dy\, \rho_G(k,y)\rho_G(k,y+\omega)[f(y) - f(\omega+y)].$$

Here $\rho_G(k,\omega)$ is the electron spectral function. With $\rho_{1,\alpha} \equiv \frac{c_0 h}{\zeta_\alpha}$, the corresponding dimensionless conductivity $\bar{\sigma}_\alpha(\omega) \equiv \rho_{1,\alpha} \times \sigma_\alpha(\omega)$ is given by

$$\bar{\sigma}_\alpha(\omega) = \left\langle \Upsilon(k,\omega)\mathcal{J}^2_\alpha(k)\right\rangle_k. \tag{7}$$

From Eqs. (6) and (7), we can see $\bar{\chi}''_\alpha(0,\omega) = \omega * \bar{\sigma}_\alpha(\omega)$

IV. PARAMETER REGION

We explore how the variation of second-neighbor hopping t', doping δ, and temperature T affects the quartet of conductivities and susceptibilities in the normal state. We focus on optimal doping or slightly overdoped cases from electron-doped (positive t') to hole-doped (negative t') systems. Our temperature region starts from 63 K to a few hundred degrees Kelvin.

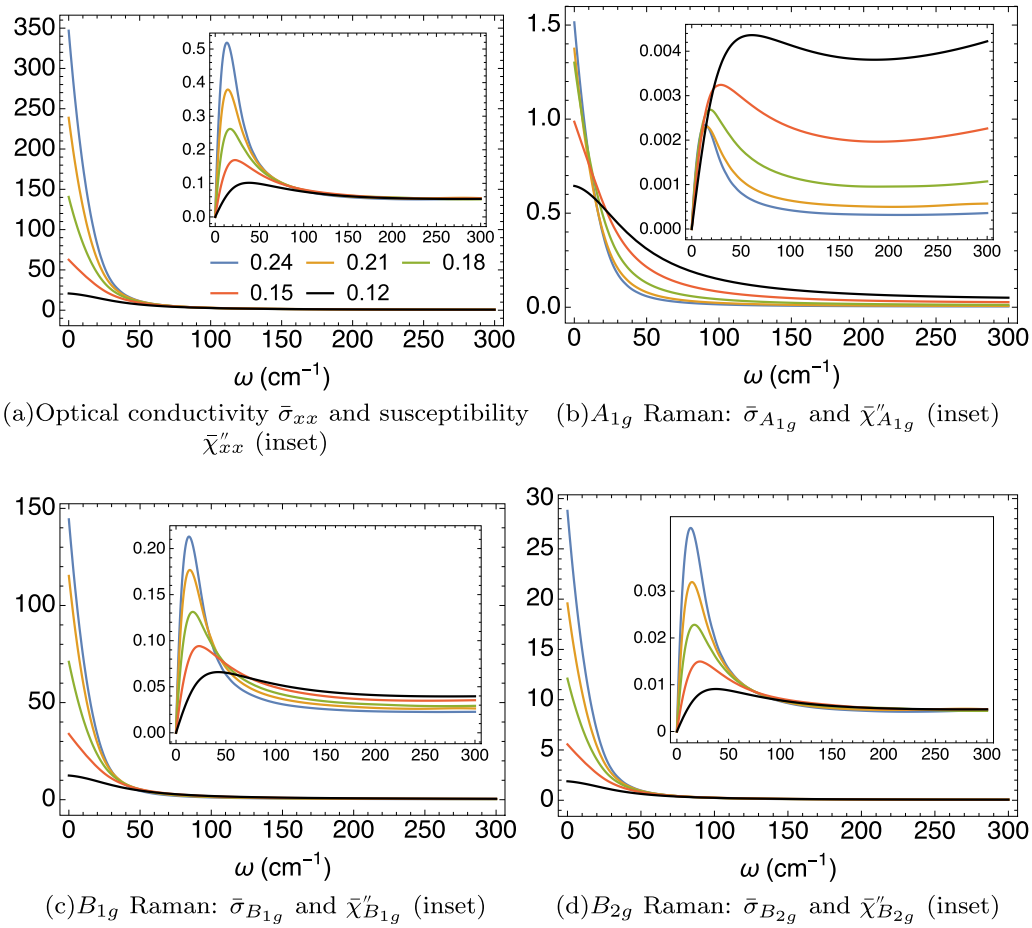

(a)Optical conductivity $\bar{\sigma}_{xx}$ and susceptibility $\bar{\chi}''_{xx}$ (inset) (b)A_{1g} Raman: $\bar{\sigma}_{A_{1g}}$ and $\bar{\chi}''_{A_{1g}}$ (inset)

(c)B_{1g} Raman: $\bar{\sigma}_{B_{1g}}$ and $\bar{\chi}''_{B_{1g}}$ (inset) (d)B_{2g} Raman: $\bar{\sigma}_{B_{2g}}$ and $\bar{\chi}''_{B_{2g}}$ (inset)

FIG. 5. Dynamical conductivities $\bar{\sigma}_\alpha$ and susceptibilities $\bar{\chi}''_\alpha$ (inset) for the electron-doped case $t' = 0.2$, $T = 63$ K at different δ, as marked.

V. DC LIMIT AND ELECTRICAL RESISTIVITY RESULTS:

Using the spectral function from the second-order ECFL theory, we calculate the dimensionless dc ($\omega \to 0$) electrical and Raman conductivities $\bar{\sigma}_\alpha$ from Eq. (7). The corresponding dimensionless resistivities are

$$\bar{\rho}_\alpha = \frac{1}{\bar{\sigma}_a} = \frac{1}{\langle \Upsilon(k,0)\mathcal{J}^2_\alpha(k)\rangle_k}. \tag{8}$$

The electrical resistivity in physical units is given by $\rho_{xx} = \bar{\rho}_{xx} \times \rho_{1,xx}$, with $\rho_{1,xx} = c_0 \frac{h}{e^2} \sim 1.71\ \mathrm{m}\,\Omega\,\mathrm{cm}$ [29].

We calculate typical quantities for the three Raman geometries and the electrical conductivity from Eq. (2) as a set of quartets below. The comparison of the figures in each set is of interest, since the different functions in the bare vertices pick out different parts of the k-space. In this paper, $t = 1$ serves as the energy unit; for the systems in mind, we estimate [29] $t \sim 0.45$ eV.

In Fig. 1, we plot dc resistivity $\bar{\rho}_{xx}$ and Raman resistivities in the dc limit $\bar{\rho}_{A_{1g}}$, $\bar{\rho}_{B_{1g}}$, $\bar{\rho}_{B_{2g}}$ varying hole doping δ and fixing $t' = -0.2$. The four figures have a roughly similar doping dependence, as suggested by the pseudo-identity. They all decrease when the doping increases, although the curvature changes more in $\bar{\rho}_{xx}$ and $\bar{\rho}_{A_{1g}}$ than the other two cases. This can be understood from Eq. (6) since they arise from the same kernel $\Upsilon(k, 0)$ with different filters. The quasiparticle peak in ρ_G, contributing most to $\Upsilon(k, 0)$, is located along the Fermi surface and gets broadened when warming up. The inset shows the corresponding squared vertex $\mathcal{J}^2_\alpha$ in the background and the Fermi surfaces at the lowest and highest dopings. The B_{1g} vertex vanishes along the line $k_x = k_y$ while the B_{2g} vertices vanish near $\{\pi, 0\}$ and $\{0, \pi\}$ points. In our calculation, both B_{1g} and B_{2g} overlap well with the peak region of the spectral function, whereas A_{1g} and the resistivity do not. This results in the difference between the T dependence of them and the other two in Fig. 1. It would be of considerable interest to study this pattern of T dependences systematically in future Raman studies.

Although all $\bar{\rho}_\alpha$ increase when reducing doping δ approaching the half-filling limit due to the suppression of quasiparticles, their magnitudes at high temperature vary considerably as a result of different vertices filtering the contribution from $\Upsilon(k, 0)$. We can understand this scale difference by evaluating the average of vertices over the shaded region in Fig. 2. The shaded region covers the Fermi surface for all chosen δ and t', and therefore it contains the most significant contribution to ρ_α.

At $t' = -0.2$, $\langle \mathcal{J}^2_{xx}\rangle_s \approx 2.41$, $\langle \mathcal{J}^2_{A_{1g}}\rangle_s \approx 0.56$, $\langle \mathcal{J}^2_{B_{1g}}\rangle_s \approx 1.30$, $\langle \mathcal{J}^2_{B_{2g}}\rangle_s \approx 0.20$, where $\langle\rangle_s$ represents the k average over the shaded region. They not only explain the relation $\bar{\rho}_{xx} < \bar{\rho}_{B_{1g}} < \bar{\rho}_{A_{1g}} < \bar{\rho}_{B_{2g}}$, but they also capture the ratio among them rather closely at high enough T. The structure at low T is more

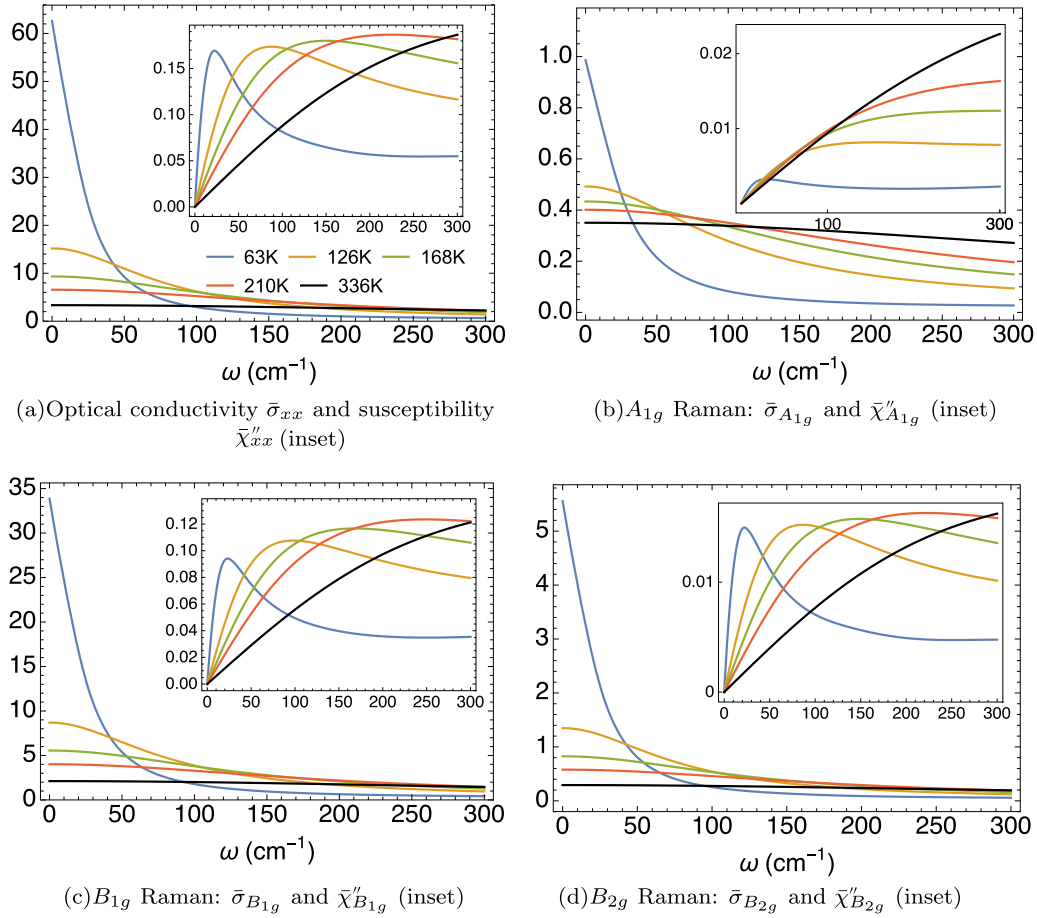

(a)Optical conductivity $\bar{\sigma}_{xx}$ and susceptibility $\bar{\chi}''_{xx}$ (inset)

(b)A_{1g} Raman: $\bar{\sigma}_{A_{1g}}$ and $\bar{\chi}''_{A_{1g}}$ (inset)

(c)B_{1g} Raman: $\bar{\sigma}_{B_{1g}}$ and $\bar{\chi}''_{B_{1g}}$ (inset)

(d)B_{2g} Raman: $\bar{\sigma}_{B_{2g}}$ and $\bar{\chi}''_{B_{2g}}$ (inset)

FIG. 6. Dynamical conductivities and (inset) susceptibilities for the electron-doped case with $t' = 0.2$, $\delta = 0.15$ for various T's as marked. Part (d) with B_{2g} symmetry is comparable to the high-resolution experimental result in Fig. 2 of Ref. [10] at a comparable set of T's. The theoretical curve reproduces well the quasielastic peaks and their T evolution.

subtle, and it carries information about the magnitude of t' that cannot be captured by the above high-T argument.

Although all $\bar{\rho}_\alpha$ increase as δ decreases in general, their t' dependence can be rather different, as shown in Fig. 3. $\bar{\rho}_{xx}$ and $\bar{\rho}_{B_{1g}}$ decrease monotonically in general as t' increases from hole-doped (negative) to electron-doped (positive), while $\bar{\rho}_{A_{1g}}$ and $\bar{\rho}_{B_{2g}}$ decrease only as $|t'|$ increases and their monotonicity with respect to t' changes upon sign change of t'. Another interesting observation is that $\bar{\rho}_\alpha(t' = -0.2) > \bar{\rho}_\alpha(t' = 0.2)$ and $\bar{\rho}_\alpha(t' = -0.4) > \bar{\rho}_\alpha(t' = 0.4)$ are generally true for $\alpha = xx$, B_{1g} and B_{2g}, but for the A_{1g} case, $\bar{\rho}_\alpha(t' = -0.2) < \bar{\rho}_\alpha(t' = 0.2)$ in general and $\bar{\rho}_\alpha(t' = -0.4) \approx \bar{\rho}_\alpha(t' = 0.4)$.

In Eq. (8), the resistivities depend on t' through $\Upsilon(k, 0)$ and $\mathcal{J}^2_\alpha$. To estimate their t' dependence, we can look at their average over the shaded region $\langle\Upsilon(k, 0)\rangle_s$ and $\langle\mathcal{J}^2_\alpha\rangle_s$. While $\langle\Upsilon(k, 0)\rangle_s$ rises monotonically as t' increases, $\langle\mathcal{J}^2_\alpha\rangle_s$ ($\alpha = xx, A_{1g}, B_{2g}$) is a quadratic function of t' that behaves differently at positive and negative t', as shown in Eq. (2).

In the simplest B_{1g} case, $\mathcal{J}^2_{B_{1g}}$ is independent of t'. Then t' only affects $\bar{\rho}_{B_{1g}}$ through $\Upsilon(k, 0)$ and therefore $\bar{\rho}_{B_{1g}}$ increases almost monotonically as t' decreases (the crossing between $t = 0.2$ and 0.4 is due to the fact that the change in Fermi surface geometry leads to a different filtering result when coupling to $\mathcal{J}^2_{B_{1g}}$). In the charge-current case, the t' dependence of $\Upsilon(k, 0)$ still dominates since $\bar{\rho}_{xx}$ behaves similarly to $\bar{\rho}_{B_{1g}}$ and the contribution from $\mathcal{J}^2_{xx}$ mostly modifies the curvature without affecting the relative scale.

The different behaviors in the other two cases indicate the quadratic t' dependence in $\mathcal{J}^2_\alpha$ ($\alpha = A_{1g}, B_{2g}$) becomes dominant. In the simpler B_{2g} case, $\mathcal{J}^2_{B_{2g}} \propto t'^2$ provides the dominant t' dependence in $\bar{\rho}_{B_{2g}}$, explaining $\bar{\sigma}_{B_{2g}}(t' = 0) = 0$ and $\bar{\rho}_{B_{2g}}(|t'| = 0.2) > \bar{\rho}_{B_{2g}}(|t'| = 0.4)$ regardless of the sign of t'. Similarly, due to the quadratic t' dependence of $\mathcal{J}^2_{A_{1g}}$, $\bar{\rho}_{A_{1g}}(t' = 0) > \bar{\rho}_{A_{1g}}(|t'| = 0.2) > \bar{\rho}_{A_{1g}}(|t'| = 0.4)$.

Typically negative t' leads to stronger correlation and suppresses the quasiparticle peak [29] and hence for a certain $|t'|$, $\bar{\rho}_\alpha(t' < 0) > \bar{\rho}_\alpha(t' > 0)$ is generally true except for the A_{1g} case. In this exception, the negative linear t' term in $\mathcal{J}^2_{A_{1g}}$ shifts the stationary point away from $t' = 0$ and counters this effect from $\Upsilon(k, 0)$ for small $|t'|$ leading to $\bar{\rho}_{A_{1g}}(t' = -0.2) < \bar{\rho}_{A_{1g}}(t' = 0.2)$ and $\bar{\rho}_{A_{1g}}(t' = -0.4) \approx \bar{\rho}_{A_{1g}}(t' = 0.4)$.

Besides, $\bar{\rho}_{A_{1g}}$ shows rather different T-dependent behaviors between electron-doped $t' \geqslant 0$ and hole-doped $t' < 0$ cases. At negative t', $\bar{\rho}_{A_{1g}}$ increases almost linearly with temperature. But at zero or positive t', $\bar{\rho}_{A_{1g}}$ first increases sharply up to a certain temperature scale depending on t' and then crosses over to a region where the growth rate becomes much smaller.

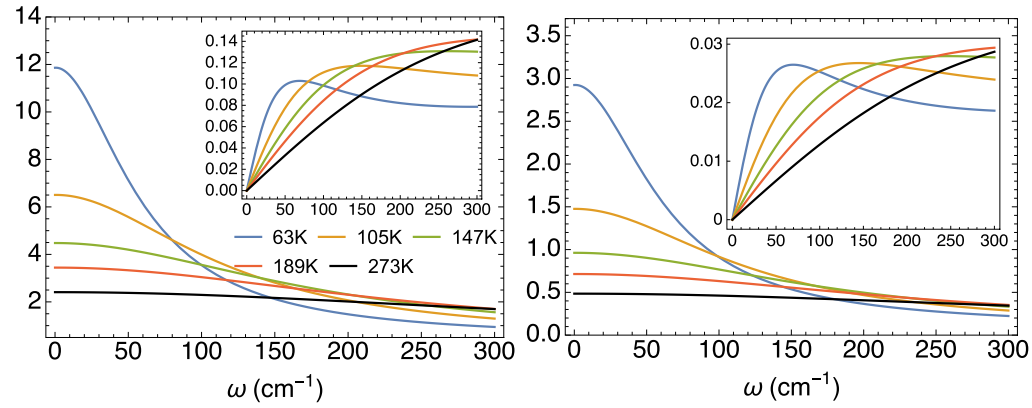

(a)Optical conductivity $\bar{\sigma}_{xx}$ and susceptibility $\bar{\chi}''_{xx}$ (inset) (b)A_{1g} Raman: $\bar{\sigma}_{A_{1g}}$ and $\bar{\chi}''_{A_{1g}}$ (inset)

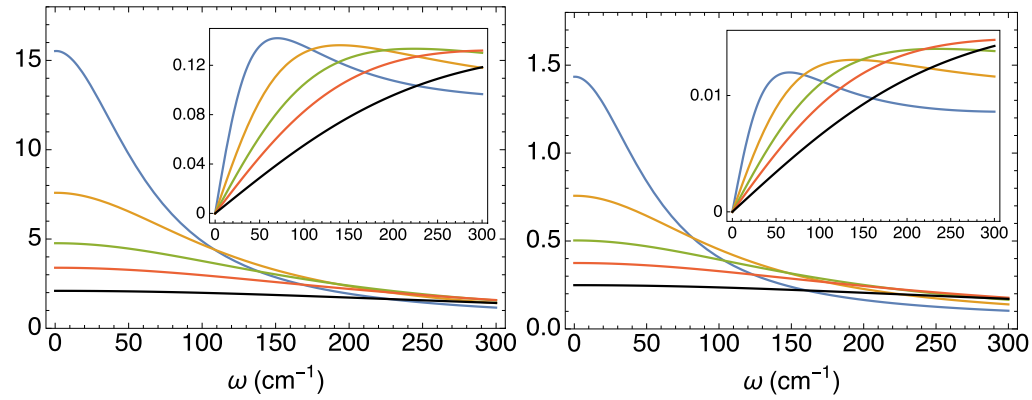

(c)B_{1g} Raman: $\bar{\sigma}_{B_{1g}}$ and $\bar{\chi}''_{B_{1g}}$ (inset) (d)B_{2g} Raman: $\bar{\sigma}_{B_{2g}}$ and $\bar{\chi}''_{B_{2g}}$ (inset)

FIG. 7. Optical conductivity $\bar{\sigma}_{xx}(\omega)$ and the Raman conductivities $\bar{\sigma}_{A_{1g}}(\omega)$, $\bar{\sigma}_{B_{1g}}(\omega)$, $\bar{\sigma}_{B_{2g}}(\omega)$ at $t' = -0.2$, $\delta = 0.15$ and varying T, as marked (same legend for all subfigures). The corresponding dimensionless susceptibility is plotted in the inset with the same x axis. References [6,7,10] show data that correspond to these variables.

VI. FINITE ω RESULTS

Next we present the ω-dependent optical and Raman conductivities defined in Eq. (7). In Figs. 4 and 5, the set of four ω-dependent conductivities are displayed for the hole-doped system at $t' = -0.2$ and the electron-doped system at $t' = 0.2$, respectively, for a set of typical densities at low T. In the insets we display the corresponding imaginary part of susceptibility, related through Eq. (6). In most cases, the quasielastic peak gets suppressed and shifts to higher frequency when reducing the carrier concentration. The only exception is $\bar{\chi}''_{A_{1g}}$ at $t' = 0.2$. Its quasielastic peaks are considerably smaller than other geometries due to the fluctuation in the specific vertex, and they get higher and broader as doping increases.

In Fig. 6 we focus on the electron-doped case of varying T at $t' = 0.2$, $\delta = 0.15$, where high-quality experimental results

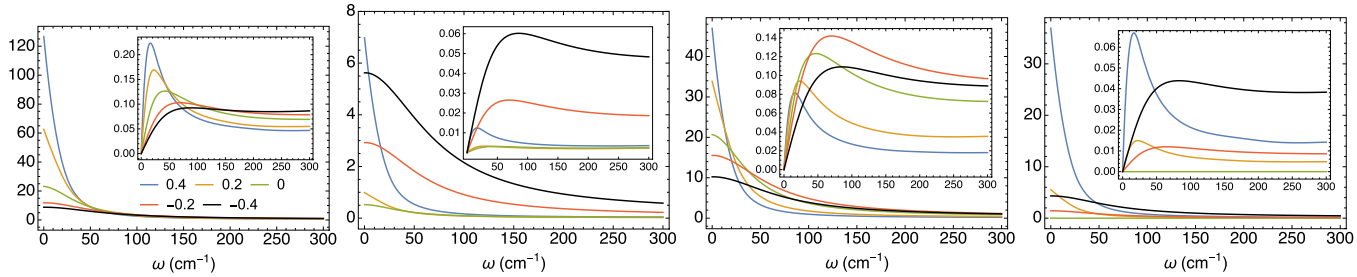

(a)Optical conductivity $\bar{\sigma}_{xx}$ and susceptibility $\bar{\chi}''_{xx}$ (inset) (b)A_{1g} Raman: $\bar{\sigma}_{A_{1g}}$ and $\bar{\chi}''_{A_{1g}}$ (inset) (c)B_{1g} Raman: $\bar{\sigma}_{B_{1g}}$ and $\bar{\chi}''_{B_{1g}}$ (inset) (d)B_{2g} Raman: $\bar{\sigma}_{B_{2g}}$ and $\bar{\chi}''_{B_{2g}}$ (inset)

FIG. 8. Optical conductivity $\bar{\sigma}_{xx}(\omega)$ and the Raman conductivities $\bar{\sigma}_{A_{1g}}(\omega)$, $\bar{\sigma}_{B_{1g}}(\omega)$, $\bar{\sigma}_{B_{2g}}(\omega)$ at $\delta = 0.15$, $T = 63$ K, and varying t', as marked (same legend for all subfigures). The corresponding dimensionless susceptibility is plotted in the inset with the same x axis. References [6,7,10] show data that correspond to these variables.

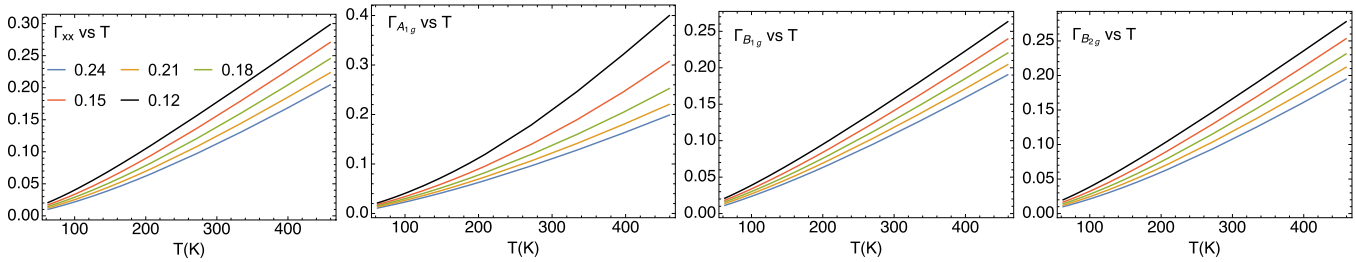

(a)Optical Relaxation rate (b)A_{1g} Raman: Relaxation rate (c)B_{1g} Raman: Relaxation rate (d)B_{2g} Raman: Relaxation rate

FIG. 9. Relaxation rates (half-widths at half-maximum) of $\sigma_\alpha(\omega)$ in units of t, at $t' = -0.2$ at various marked δ. The optical rate shows less convexity than the corresponding dc resistivity of Ref. [29]. The rates in (a,b) and (c,d) have similar orders of magnitude, for reasons discussed in Fig. 1.

are available for the B_{2g} Raman channel in Ref. [10]; see particularly Fig. 2. We evaluate the susceptibility at T values corresponding to those in this experiment. There is a fair similarity between the theoretical curve [panel (d)] and the experiment. In particular, the theoretical curve reproduces the quasielastic peak and its T evolution. The other three panels in Fig. 6 are our theoretical predictions, and they are equally amenable to experimental verification.

In the xx, B_{1g}, B_{2g} geometries, the quasielastic peaks in susceptibility get slightly higher and quite broader upon warming. The A_{1g} case is different. Its quasielastic peaks are much less obvious (too broad) except for the lowest temperature, and the peak magnitude is rather sensitive to temperature increase.

We also vary T at hole doping $t' = -0.2$ in Fig. 7. Comparing with the electron-doped case in Fig. 6, we note that the hole-doped optical and Raman objects share a greater similarity in shape dependence on T if we ignore the scale difference. As T increases, the quasiparticle peaks get softened, and hence it generally suppresses the conductivities as well as the quasielastic peak in susceptibilities.

For completeness, the t' variation in $\bar{\sigma}_\alpha(\omega)$ and $\bar{\chi}''_\alpha(\omega)$ is plotted in Fig. 8, and it looks rather different among various geometries. This can be understood as arising from the competition among various factors. We have a quadratic t' dependence in the squared vertices, and a monotonic t' dependence in the magnitude and geometry of $\Upsilon(k, \omega)$. The t' dependence of the shape of $\bar{\sigma}_\alpha$ has more commonality. Another interesting observation is that, unlike the dc case when $\bar{\sigma}_{xx}$ and $\bar{\sigma}_{B_{1g}}$ are similarly affected by t', at finite frequency their behaviors depend on t' rather differently. This difference is more obviously observed in terms of $\bar{\chi}''$.

From the optical and Raman conductivities $\bar{\sigma}_\alpha$ we can extract a frequency scale Γ_α, as the half-width at half-maximum, in units of t. These are plotted against T in Fig. 9 for varying δ and Fig. 10 for varying t'. It is remarkable that despite a bare bandwidth of ~ 3.6 eV, these frequency scales appear close to linear in T down to very low T. This is closely related to the observation in Ref. [29] that the resistivity departs from a T^2 behavior at extraordinarily low T's, i.e., the effective Fermi temperatures are suppressed from the bare values by two or more orders of magnitude. Although the magnitude of the optical and Raman conductivities differs a lot, their relaxation rates describing the shape turn out to be much closer, as a result of a similar T-dependent line shape of the spectral function [29] in the normal state.

VII. CONCLUSION AND DISCUSSION

We have presented calculations of the electrical and Raman resistivities in the dc limit, the optical conductivity, the Raman susceptibilities, and related objects based on the second-order ECFL theory in Ref. [29]. We computed the susceptibilities (using the leading-order approximation) with the shown results. Experiments on different geometries can test and put some bound on this hypothesis of weak vertex corrections for the Raman operators. This is clearly of theoretical importance, since going beyond the bubble graphs brings in a formidable level of complexity.

The ECFL theory leads to a very small quasiparticle weight Z and a large background extending over the bandwidth, and it has a very small effective Fermi temperature leading to an interesting T dependence of the resistivity, as discussed in [29]. The line shape of the calculated Raman susceptibility is close to that for the case of electron-doped NCCO [10] in terms of the T and ω dependences, and therefore it is promising. Our calculation also gives the Raman susceptibility in two other

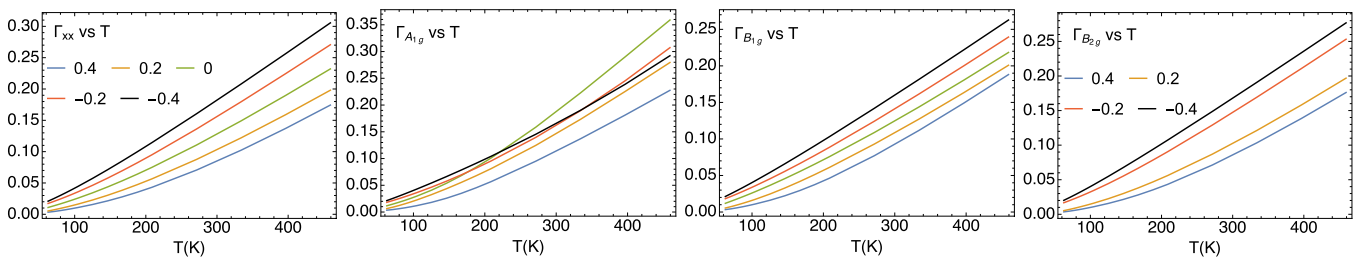

(a)Optical Relaxation rate (b)A_{1g} Raman: Relaxation rate (c)B_{1g} Raman: Relaxation rate (d)B_{2g} Raman: Relaxation rate

FIG. 10. The half-width at half-maximum for optical conductivity and Raman conductivities at $\delta = 0.15$ and varying t', as marked.

geometries, and this prediction can be checked against future experiments that are quite feasible. We note that the data [6] from Sugai *et al.* for this quartet of variables in the case of LSCO seem to be roughly consistent with our results, and a more detailed comparison is planned.

The focus on the T dependence in the $\omega \to 0$ limit, i.e., on resistivities, can be quite a fruitful goal for future experiments, since this limit gets rid of all excitations and measures the "pure background." It is an important exercise since the different geometries probe different combinations of t, t' as they occur in the bare vertices [Eq. (2), as stressed above. We are predicting that the Raman resistivity in each channel can be found from the intensity at low T, and broadly speaking it is similar to resistivity. In further detail, it is predicted to be (a) channel-specific and (b) t'/t-dependent. These clear-cut predictions can be tested in future experiments.

Finally, although such a measurement is not commonly done, a systematic measurement of the ratios of the scattering cross sections in different geometries should be feasible. This measurement, and a comparison between the quartet of susceptibilities presented here, can be profitably compared with recent theories of strongly correlated systems to yield material parameters. Most importantly, it can yield physical insights into the mechanism underlying the broad nonresonant Raman signals that have remained quite mysterious so far.

ACKNOWLEDGMENTS

We thank Tom Devereaux, Lance Cooper, and Girsh Blumberg for helpful discussions. The computation was done on the comet in XSEDE [32] (TG-DMR170044) supported by National Science Foundation Grant No. ACI-1053575. The work at UCSC was supported by the U.S. Department of Energy (DOE), Office of Science, Basic Energy Sciences, under Award No. DE-FG02-06ER46319.

[1] H. A. Kramers and W. Heisenberg, Z. Phys. **31**, 681 (1925).
[2] P. A. Wolff, Phys. Rev. **171**, 436 (1968).
[3] P. A. Wolff and P. Platzmann, *Solid State Physics* (Academic Press, New York, 1973), Suppl. 13; W. Hayes and R. H. Loudon, *Scattering of Light by Crystals* (Wiley, New York, 1978).
[4] A. A. Abrikosov and V. M. Genkin, Sov. Phys. JETP **38**, 417 (1974).
[5] S. Sugai, S. I. Shamoto, and M. Sato, Phys. Rev. B **38**, 6436 (1988).
[6] S. Sugai, Y. Takayanagi, N. Hayamizu, T. Muroi, J. Nohara, R. Shiozaki, K. Okazaki, and K. Takenaka, Physica C **470**, S97 (2010).
[7] S. Sugai, J. Nohara, R. Shiozaki, T. Muroi, Y. Takayanagi, N. Hayamizu, K. Takenaka, and K. Okazaki, J. Phys.: Condens. Matter **25**, 415701 (2013).
[8] R. Hackl, L. Tassini, F. Venturini, C. Hartinger, A. Erb, N. Kikugawa, and T. Fujita, in *Advances in Solid State Physics*, edited by B. Kramer (Springer-Verlag, Berlin, Heidelberg, 2005), Vol. 45, pp. 227–238.
[9] M. M. Qazilbash, A. Koitzsch, B. S. Dennis, A. Gozar, H. Balci, C. A. Kendziora, R. L. Greene, and G. Blumberg, Phys. Rev. B **72**, 214510 (2005).
[10] A. Koitzsch, G. Blumberg, A. Gozar, B. S. Dennis, P. Fournier, and R. L. Greene, Phys. Rev. B **67**, 184522 (2003).
[11] C. Sauer and G. Blumberg, Phys. Rev. B **82**, 014525 (2010).
[12] M. V. Klein and S. B. Dierker, Phys. Rev. B **29**, 4976 (1984).
[13] M. V. Klein, S. L. Cooper, A. L. Kotz, R. Liu, D. Reznik, F. Slakey, W. C. Lee, and D. M. Ginsberg, Physica C **185**, 72 (1991); G. Blumberg and M. V. Klein, J. Low Temp. Phys. V **117**, 1001 (1999).
[14] F. Slakey, S. L. Cooper, M. V. Klein, J. P. Rice, and D. M. Ginsberg, Phys. Rev. B **39**, 2781 (1989).
[15] S. L. Cooper, D. Reznik, A. Kotz, M. A. Karlow, R. Liu, M. V. Klein, W. C. Lee, J. Giapintzakis, D. M. Ginsberg, B. W. Veal, and A. P. Paulikas, Phys. Rev. B **47**, 8233 (1993).
[16] S. L. Cooper, F. Slakey, M. V. Klein, J. P. Rice, E. D. Bukowski, and D. M. Ginsberg, J. Opt. Soc. Am. B **6**, 436 (1989).
[17] S. L. Cooper, M. V. Klein, B. G. Pazol, J. P. Rice, and D. M. Ginsberg, Phys. Rev. B **37**, 5920 (1988).
[18] B. S. Shastry and B. I. Shraiman, Phys. Rev. Lett. **65**, 1068 (1990).
[19] B. S. Shastry and B. I. Shraiman, Int. J. Mod. Phys. B **5**, 365 (1991).
[20] J. K. Freericks and T. P. Devereaux, Phys. Rev. B **64**, 125110 (2001); J. K. Freericks, T. P. Devereaux, M. Moraghebi, and S. L. Cooper, Phys. Rev. Lett. **94**, 216401 (2005).
[21] T. P. Devereaux and R. Hackl, Rev. Mod. Phys. **79**, 175 (2007).
[22] L. de Medici, A. Georges, and G. Kotliar, Phys. Rev. B **77**, 245128 (2008).
[23] J. Kosztin and A. Zawadowski, Solid State Commun. **78**, 1029 (1991).
[24] B. S. Shastry, Phys. Rev. Lett. **107**, 056403 (2011).
[25] B. S. Shastry and E. Perepelitsky, Phys. Rev. B **94**, 045138 (2016).
[26] B. S. Shastry, E. Perepelitsky, and A. C. Hewson, Phys. Rev. B **88**, 205108 (2013).
[27] P. Mai, S. R. White, and B. S. Shastry, Phys. Rev. B **98**, 035108 (2018).
[28] R. Žitko, D. Hansen, E. Perepelitsky, J. Mravlje, A. Georges, and B. S. Shastry, Phys. Rev. B **88**, 235132 (2013); E. Perepelitsky and B. S. Shastry, Ann. Phys. (N.Y.) **338**, 283 (2013).
[29] B. S. Shastry and P. Mai, New J. Phys. **20**, 013027 (2018).
[30] P. Mai and B. S. Shastry, arXiv:1808.09788 (2018).
[31] Parabolic bands leads to an exact cancellation, whereby the A_{1g} scattering is unobservable. References [3,4,18,19] show that the cancellation is inoperative with nonparabolic bands, or with disorder. Experimentally, Fig. 2 of Ref. [6] shows an A_{1g} contribution similar in scale to the other two geometries.
[32] J. Towns *et al.*, Comput. Sci. Eng. **16**, 62 (2014).